

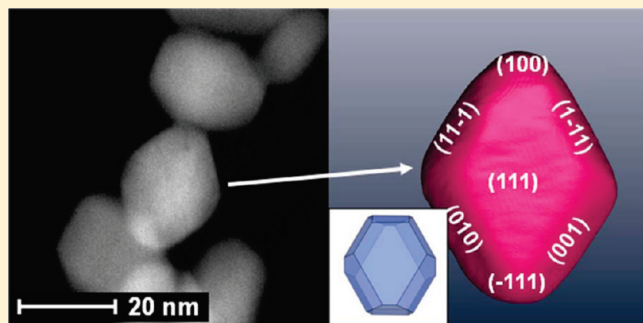
Three-Dimensional Structure of CeO₂ Nanocrystals

Joyce Pei Ying Tan,[†] Hui Ru Tan,[†] Chris Boothroyd,[‡] Yong Lim Foo,[†] Chao Bin He,[†] and Ming Lin^{†,*}

[†]Institute of Materials Research and Engineering, A*STAR (Agency for Science, Technology and Research), 3 Research Link, S117602, Singapore

[‡]Center for Electron Nanoscopy, Technical University of Denmark, DK-2800 Lyngby, Denmark

S Supporting Information



1. INTRODUCTION

The surfaces and 3-dimensional (3D) structures of nanomaterials significantly impact their ultimate performance in the application of catalysis, biosensors, microelectronics, and data storage, etc.^{1,2} Over the past decade, great progress has been made on the shape-controlled synthesis of inorganic materials by delicate synthetic approaches, especially for the materials based on face-centered cubic (fcc) crystal packing, including metals (Ag, Au, Pt, bimetals)^{3–7} and metal oxide materials (Cu₂O, CeO₂, Fe₃O₄ etc.).^{8–10} Nanocrystals with fcc structures always formed in polyhedral shapes bounded by the low-energy surfaces, such as the {100}, {110}, and {111}. By changing the surface anisotropy of crystals with the experimental conditions and the addition of various surfactants, the different growth rate of the different planes will result in the formation of nanocrystals with controlled shapes, such as cubic, truncated cubic, cuboctahedron, truncated octahedron, octahedron, and other irregular shapes.¹¹

Although tremendous studies have been carried out on the shape-controlled synthesis of nanocrystals, the characterization of surface and 3D structures of the particles obtained at nanometer scale is still a major challenge. A detailed and atomic level understanding of the surface and morphology of nanoparticles

will allow us to take a step forward to better control the shapes, structures, and properties of particles as well as reveal the growth mechanism to achieve a green synthesis route. Presently, the 3D shape of particles larger than 50 nm can be visualized directly by scanning electron microscope (SEM), but the smaller ones are mostly imaged using the transmission electron microscope (TEM). Since TEM images are 2D projections of 3D objects, the information collected from TEM images may not reflect the true 3D structure. This can be overcome by observing the specimen from different viewing angles in the microscope. More information can be disclosed by titling samples to different zone axes. However, some 2D images are still difficult to interpret because they require a good understanding of crystallography and sufficient prior knowledge of the structure of the sample. Therefore, electron tomography has been developed to support interpretation by reconstructing a 3D model of the object.^{12–19} Using tomography, a 3D structure can be reconstructed from a tilt series of 2D images. The resolution of electron tomography can be as small as 1 nm,^{14,15} making it an appropriate technique

Received: September 27, 2010

Revised: January 7, 2011

Published: February 15, 2011

to resolve complex 3D geometries and characterize the internal crystal structures of materials at nanometer scale.

Ceria (CeO_2) is an important oxide material with the fcc fluorite structure. It has multiple applications, such as working as a promoter in commercial catalysts to reduce the emissions of CO, hydrocarbon, and NO_x from automobile exhausts;^{20–22} being an oxygen ion conductor in solid fuel cells;^{23,24} and serving as a UV adsorption material in UV blocking and shielding products.^{25,26} Interestingly, it has been found that the catalytic performance of CeO_2 nanoparticles is strongly dependent on the facets exposed.^{20,21} Theoretical simulations have indicated that the stabilities of the surface follow the order $\{111\} > \{110\} > \{100\}$,^{27,28} whereas the catalytic reactivity for the oxidation of CO to CO_2 on the corresponding surface is reversed.²⁷

Recent materials research on CeO_2 particles has been focused on the shape selective synthesis of CeO_2 particles with controlled morphologies (dots,^{20,29–33} cubes,^{34–36} nanorods,^{37,38} nanowires,³⁹ etc.) and investigations of the connection between the 3D structures and their catalytic activities of the corresponding exposed surface.^{30,34,35,38} For example, it has been suggested that polyhedral CeO_2 particles are always in the form of octahedra and truncated octahedra.^{28–34} With the help of electron tomography, it has been revealed that the 3D shape of CeO_2 nanocubes is composed predominantly of $\{001\}$ facets with $\{111\}$ corners and $\{110\}$ edge truncations. Two research groups have synthesized CeO_2 nanorods with exposed $\{100\}$ and $\{110\}$ planes, which have shown higher activities for the oxidation of CO.^{35,38}

Although some progress has been made on the shape selective synthesis of CeO_2 nanoparticles, the complete characterization of the detailed structure of the particles obtained is still challenging, and a systematic understanding of the 3D structure and the surfaces of CeO_2 nanocrystals by conventional synthesis methods is still lacking. Moreover, the CeO_2 particles fabricated by shape controlled methods (such as rods, cubes, etc.) are not in a thermodynamically stable form and will transform into stable configurations (such as octahedra) when undergoing high-temperature annealing for commercial usage.²⁰ In this paper, motivated by the challenge of characterizing the surface structures of nanocrystalline CeO_2 particles at nanoscale, we present the surface and 3D shape of hydrothermally synthesized CeO_2 nanoparticles using HRTEM imaging and electron tomography. The aggregation mechanism of nanosized CeO_2 particles is also discussed through morphology analysis.

2. EXPERIMENTAL SECTION

2.1. Synthesis of CeO_2 Nanoparticles. A hydrothermal method was used for the synthesis of our CeO_2 nanocrystals. One millimole of $\text{Ce}(\text{NO}_3)_3 \cdot 6\text{H}_2\text{O}$ was dissolved in 30 mL of PVP/ethanol (polyvinylpyrrolidone (PVP) 30 g/L, molecular weight 30 000) solution and then mixed with 3 mmol of NaOH. The mixture was stirred continuously for 10 min and transferred into a 50 mL stainless steel atom reactor from Fisher Scientific. The reactor was then heated in an oven at 200 °C under autogenous pressure for 24 and 48 h, and then cooled to room temperature. The final products were collected after centrifuging and washing several times with deionized water to remove the residual reactants. The washed CeO_2 product from the 24 h hydrothermal process was again dispersed in 30 mL of ethanol solution and received another 24 h of hydrothermal treatment at 200 °C.

2.2. Materials Characterization. The synthesized CeO_2 nanocrystals were dispersed in ethanol and dropped onto copper

grids coated with a layer of ultrathin carbon film (from Ted Pella) or lacey carbon film (from SPI). Structural analysis and 3D electron tomography of as-synthesized CeO_2 nanoparticles was performed on a JEOL 2100 (200 kV) TEM and an FEI Titan 80/300 S/TEM (scanning/transmission electron microscope) (300 kV) that is equipped with a high-angle annular dark-field (HAADF) detector, a monochromator, and a single-tilt tomography holder. A total of 71 HAADF–STEM images for STEM tomography were collected over a tilt range of -70° to 70° , with 2° tilt steps. The stage tilting and image acquisition were done automatically by the FEI Xplore-3D tomography program, and the tracking and refocusing of the area of interest were carried out manually to shorten the total acquisition time, minimize the beam damage to the sample, and reduce the build-up of contaminants under prolonged beam irradiation. The magnification was 710 000 times, corresponding to 0.17 nm per pixel. The acquisition time for one 1024×1024 sized image was 24 s. The final tilt series data was aligned using a cross-correlation method and reconstructed by the simultaneous iterative reconstruction technique (SIRT, 30 iterations) using Inspect3D, and the reconstructed 3D volume was visualized by surface and voxel rendering using Amira 4.1.

3. RESULTS AND DISCUSSION

Figure 1 shows typical TEM images from the ceria nanoparticles and their corresponding size distributions. A random selection of 100 particles was used for the size statistics for each sample. Diffraction patterns obtained from these samples can be assigned to the fcc fluorite structure with a lattice constant of 0.54 nm. Most of the nanometer sized CeO_2 particles are single crystals with little agglomeration. The particle size and shape can be controlled by the duration of the hydrothermal treatment and passivation of the surfactant (PVP). With the addition of PVP molecules, a narrower CeO_2 particle size distribution can be achieved. This is because the adsorption of PVP molecules on the CeO_2 surface helps to stabilize the CeO_2 nucleus, control the nucleus growth rate, and prevent the aggregation between particles by steric hindrance.³⁴ The mean particle size is 5.0 nm (17% std dev (SD) in Figure 1a) and 6.8 nm (23% SD in Figure 1b) after 24 and 48 h hydrothermal treatment with PVP passivation. Although the particles exhibit similar shapes, the longer reaction time results in the formation of CeO_2 nanoparticles with fewer defects, sharper edges and higher crystallinity, which is confirmed by the higher image contrast and stronger diffraction rings shown by samples in Figure 1b (larger diffraction patterns are shown in Figure S2 in the Supporting Information).

When the fresh CeO_2 particles are cleaned with water to remove PVP molecules and treated with another 24 h of hydrothermal heating, the average CeO_2 particle size increases to 19.3 nm due to the aggregation of small CeO_2 crystallites (Figure 1c). The standard deviation was dramatically increased to 30%, indicating a less homogeneous size distribution compared with the samples with addition of PVP.

From the TEM images, it can be seen that single-crystal CeO_2 nanoparticles with controlled size and morphology can be synthesized using the hydrothermal process. However, the TEM images demonstrate irregular 2D projections of randomly oriented 3D CeO_2 particles. To fully understand the chemical and physical properties of the CeO_2 products, the actual shape and surface morphology were investigated carefully by HRTEM and

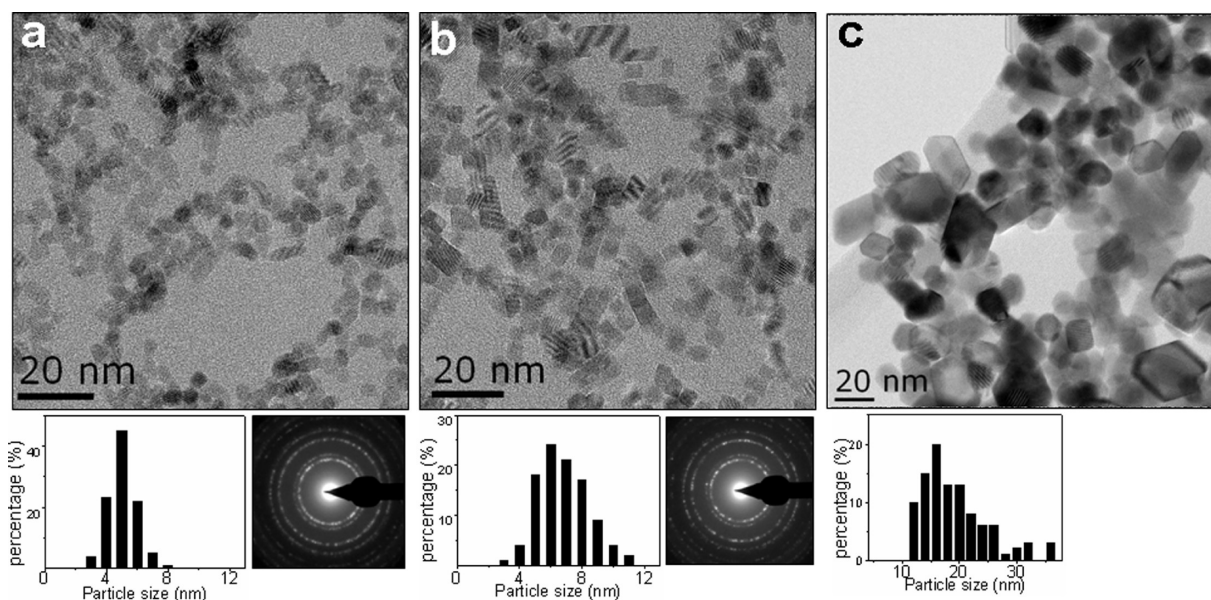


Figure 1. Bright-field TEM images of hydrothermally grown CeO_2 nanoparticles (a) after 24 h of treatment with PVP (b) after 48 h of treatment with PVP. (c) Particles as in panel a after cleaning with water and another 24 h of hydrothermal treatment without PVP. The insets show a selected area diffraction pattern and the corresponding particle size distributions.

electron tomography to be able to correlate their shapes with their properties.

3.1. Shape of the Smaller CeO_2 Particles after Addition of PVP. As shown in Figure 2, the 3D shape of the particles obtained with 48 h of treatment is investigated using HRTEM images acquired over a range of sample tilt angles. The particle appears to be a square shape when projected at a sample tilt of 0° . When rotated to -20° or -30° , the particle is oriented near to the $[110]$ zone axis. In this orientation (Figure 2b and c), the CeO_2 $\{111\}$ planes (spacing 0.31 nm) and $\{002\}$ planes (spacing 0.27 nm) are visible. When the particle is rotated 20° along the $[001]$ direction (Figure 2f), the $\{100\}$ side facets and the $\{110\}$ edges are exposed. The intensity profile across the particle (inset, Figure 2f) suggests the particle has a plateau perpendicular to the $[001]$ zone axis. Thus, the CeO_2 nanoparticles synthesized using the hydrothermal method with PVP passivation have a truncated octahedral shape, which is in agreement with previous TEM observations.^{29–34} The truncated octahedron has eight hexagonal $\{111\}$ facets and six square $\{001\}$ facets on the surface, as shown in Figure 3.

It is interesting to note that the six $\{001\}$ facets of the particle are not identical to one another, which can be assigned to the different growth rates between the $\{111\}$ and $\{001\}$ planes. The pictures below each TEM image in Figure 2 are drawings of the truncated octahedral particle at the corresponding tilt angle. The balls represent the Ce cations, and the red ones represent the top-most exposed Ce atoms on the $\{001\}$ surfaces. These diagrams agree very well with the lattice resolved images of the particle, providing further evidence for its truncated octahedral structure.

A careful examination of the HRTEM images reveals the existence of surface steps on the $\{111\}$ surface when viewed along the $[110]$ direction, as indicated by arrows in Figure 2b and c. Larger-sized versions of Figure 2b, c, and h are shown in Figure S3 in the Supporting Information. The steps can further be determined as $\{001\}$ type microfacets with a height of 1–2 atomic layers when viewed at a tilt angle of 50° . The formation of steps with $\{001\}$ microfacets is a result of the low surface diffusion

and incomplete rearrangement of atoms during the hydrothermal process. The presence of steps and microfacets on the $\{111\}$ surface plays a key role in catalytic reactions and provides stable and active nucleation sites for supported metal catalyst particles.

3.2. Shape of the Large CeO_2 Particles. In addition to the CeO_2 particles prepared by PVP passivation discussed above, the larger CeO_2 particles (Figure 1c) have a totally different morphology as determined from HRTEM images and 3D electron tomography. To a first approximation, the particles can be classified into two types according to their shape. A small fraction of the particles have a symmetrically truncated octahedral shape, as demonstrated in Figure 4a, whereas the majority are in the form of irregularly truncated octahedra with two nonsymmetrical $\{111\}$ and $\{\bar{1}\bar{1}1\}$ surfaces (Figure 4b). The occurrence of two nonidentical surfaces is caused by the different growth rates of the $\{111\}$ family of facets. Thus, the compressed truncated octahedron in Figure 4b is formed with 13 fewer $\{111\}$ atomic layers along $\{\bar{1}\bar{1}1\}$ than for a regular octahedron when viewed along the $[110]$ zone axis. The relative growth rate of the $\{001\}$ facets to the $\{111\}$ and $\{\bar{1}\bar{1}1\}$ facets (a/b) for this particle is calculated to be 1.04 and 1.57 respectively.

Figure 4c shows a particle orientated along $[100]$, where the truncated $\{001\}$ surfaces and four $\{110\}$ edges can be clearly observed. Figure 4d depicts the corresponding 3D structure of this particle from HRTEM image analysis. The sides highlighted in red on the $\{\bar{1}\bar{1}1\}$ and $\{1\bar{1}\bar{1}\}$ surfaces indicate the missing parts on the particle. As a result, an irregular compressed truncated octahedron is formed.

To gain a better understanding of the particles' shapes and morphologies, electron tomography was used to reveal the detailed structure unambiguously. To fulfill the projection requirement for tomography, the intensity of the 2D images should be proportional to the mass–thickness.^{14,15} Two imaging modes can be used: bright-field TEM and HAADF–STEM images. Bright-field images are not suitable for tomographic reconstruction of crystalline materials due to the presence of strong diffraction contrast when the crystals are imaged along major zone axes. For example, the particle in Figure 2 is darker when at [001]

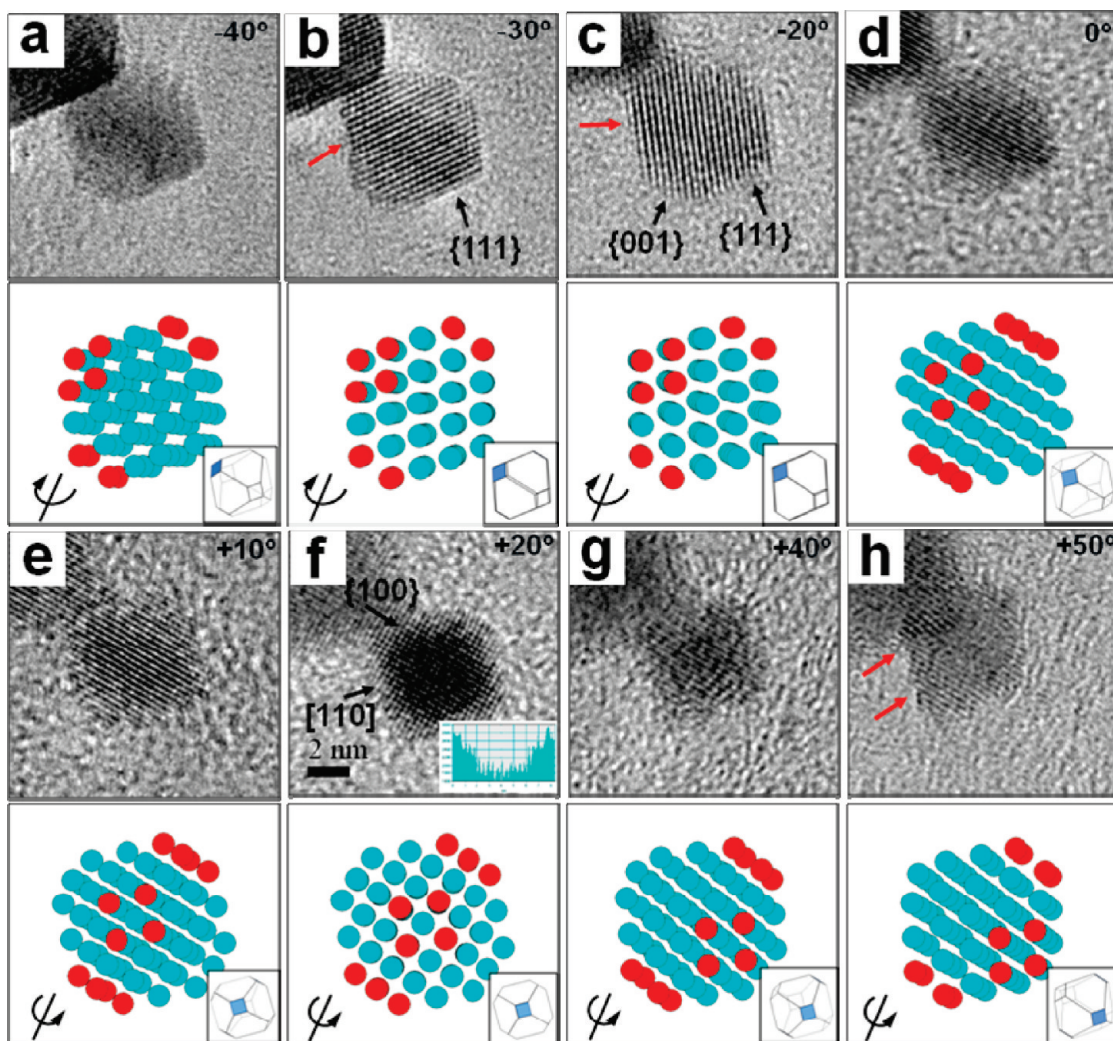


Figure 2. HRTEM images at different tilt angles and corresponding schematic drawings of a CeO₂ nanocrystal prepared with a 48 h hydrothermal process. The red balls represent the exposed atoms on the {001} surface. The tilt axis and direction is shown at the bottom-left corner. The inset in panel f shows a line profile across the particle that strongly indicates the presence of a plateau perpendicular to the [001] zone axis.

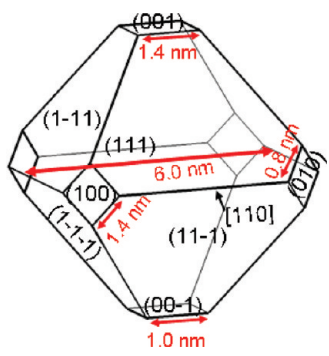


Figure 3. Schematic illustration of the CeO₂ particle shown in Figure 2.

(Figure 2f) than at other orientations away from zone axes. This nonprojection-induced phase contrast in bright-field images complicates tomographic reconstruction and leads to a distortion in the shape. HAADF-STEM images suffer less from diffraction contrast than bright-field images¹⁵ and, thus, have been used here.

Figures 5a and 5b show bright-field and HAADF-STEM images of the same CeO₂ nanocrystals. The nonprojection-induced contrast shown in the bright-field image (Figure 5a), such as Fresnel fringes seen at the edge of the particles and artifacts due to the defocus and different specimen height, are not observed in the STEM image (Figure 5b). Moreover, the interference of the carbon membrane is also substantially minimized in the HAADF-STEM image due to its low atomic number. An iso-surface rendering of the reconstructed 3D structure of the particles is depicted in Figure 5c and d. Considering the image acquisition parameters and curvature of the corners and edges of the reconstructed particles, the resolution of the tomogram is about 1–1.5 nm. We would like to point out that the surface of the CeO₂ particles appears to be flat here because the height of surface steps is smaller than the tomographic resolution. To better interpret the tomographic results of the aggregated particles and identify the surface structures, a segmentation process was applied to distinguish the two particles, A and B, shown from Figure 5e to 5l. The resolution of the tomogram after segmentation is reduced due to the application of surface smoothing. However, the segmentation process is the prerequisite for the surface

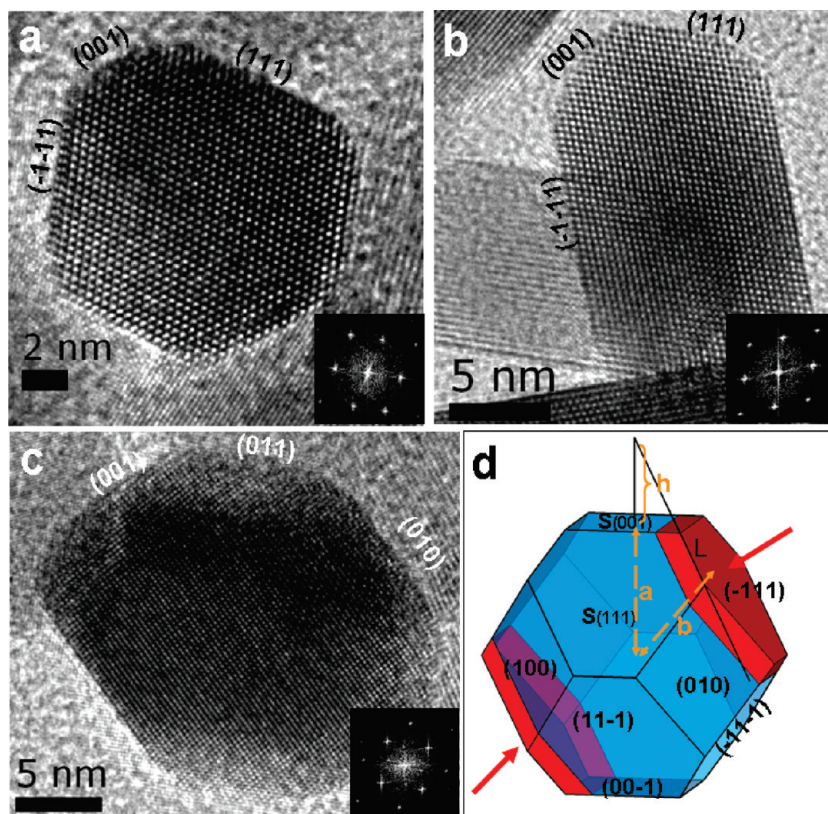


Figure 4. (a) A representative symmetrically truncated octahedral CeO₂ particle. (b) An irregular truncated octahedral CeO₂ particle viewed along [110]. (c) A CeO₂ particle orientated along [100]. (d) Diagram of the particle in panel b showing how the compressed truncated octahedral shape is formed.

model generation of individual particles, and the structures are almost the same as the iso-surface rendering results in Figure 5c and 5d. A movie showing the reconstructed 3D volume is available in the Supporting Information.

Although the particles A and B have distinctive morphology, the tomography results clearly exhibit that both particles have an irregular truncated octahedral structure, with eight {111} and six {100} facets. Particle A is compressed along the [111] and [111̄] directions, giving rise to a flat crystal with (111) and (111̄) as the largest facets, followed by the (010), (010̄), (001), and (001̄) facets. The truncated area of the (001), (001̄), (010), and (010̄) facets is larger than for regular octahedral particles, indicating more {001} facets are exposed by this structural configuration.

The compression of particle B has occurred along the [111], [111̄], [111̄], and [111̄] directions. It is noteworthy that the (100) plane of particle A is attached to the (111̄) plane of particle B. The random stacking of the particles indicates little agglomeration has occurred in the solution. Viewing of the reconstructed 3D models along ⟨110⟩ and ⟨100⟩ directions in Figure 5f, g, j, and k illustrates the real 3D structures of the irregular compressed octahedral CeO₂ particles, in accordance with the 2D TEM images. We would like to emphasize that the 2D TEM images in Figure 4b and c could demonstrate the same periphery as the projections from 3D reconstructions, but they would not be able to distinguish the surfaces that are perpendicular to the viewing directions. This unambiguously exhibits the existence of a large truncated (010) facet on the surface in comparison with smaller truncations in regular octahedral CeO₂ particles in Figure 2.

3.3. Discussion of the Growth Mechanism of CeO₂ Nanocrystals. Minimizing the surface energy is the process that drives crystallization toward a specific morphology and crystal form. CeO₂ has a fluorite structure with an fcc array of cubes consisting of one Ce⁴⁺ cation surrounded by eight O²⁻ anions with each O²⁻ anion residing in the tetrahedral interstices of four Ce ions. Theoretical simulations show that the surface energies of the CeO₂ {111} and {001} plane are 1.54 and 3.25 J/m² respectively.²⁷ According to the Wulff construction,⁴⁰ the thermodynamically stable shape for CeO₂ is a regular octahedron without any corners truncated by {001} facets. The build-up of Wulff construction and detail analysis is presented in the Supporting Information. Therefore, the higher stability of the {111} plane results in the nucleation and formation of regular truncated octahedral CeO₂ particles, with the most stable morphology having predominantly exposed {111} planes and small truncations of {001} planes at the corners.

Slight differences in the growth rates between the different {111} facets and {001} facets will lead to the formation of unequal truncated corners. Assuming a regular truncated octahedron, the area of the {001} facet increases with the enlargement of the corner or the height (*h*) of the truncated pyramid (Figure 4d). The growth rate along ⟨001⟩ to that of ⟨111⟩ should be

$$a/b = 1.73 - 2.45 h/L \quad (0 \leq h/L \leq 0.35) \quad (1)$$

where *L* is the side length of the octahedron and the range of *h/L* is from 0 to 0.35, with the shape changing from octahedron (*a/b* = 1.73) to truncated octahedron ($0.87 < a/b < 1.73$), to cuboctahedron (*a/b* = 0.87). The area of the (111) and truncated

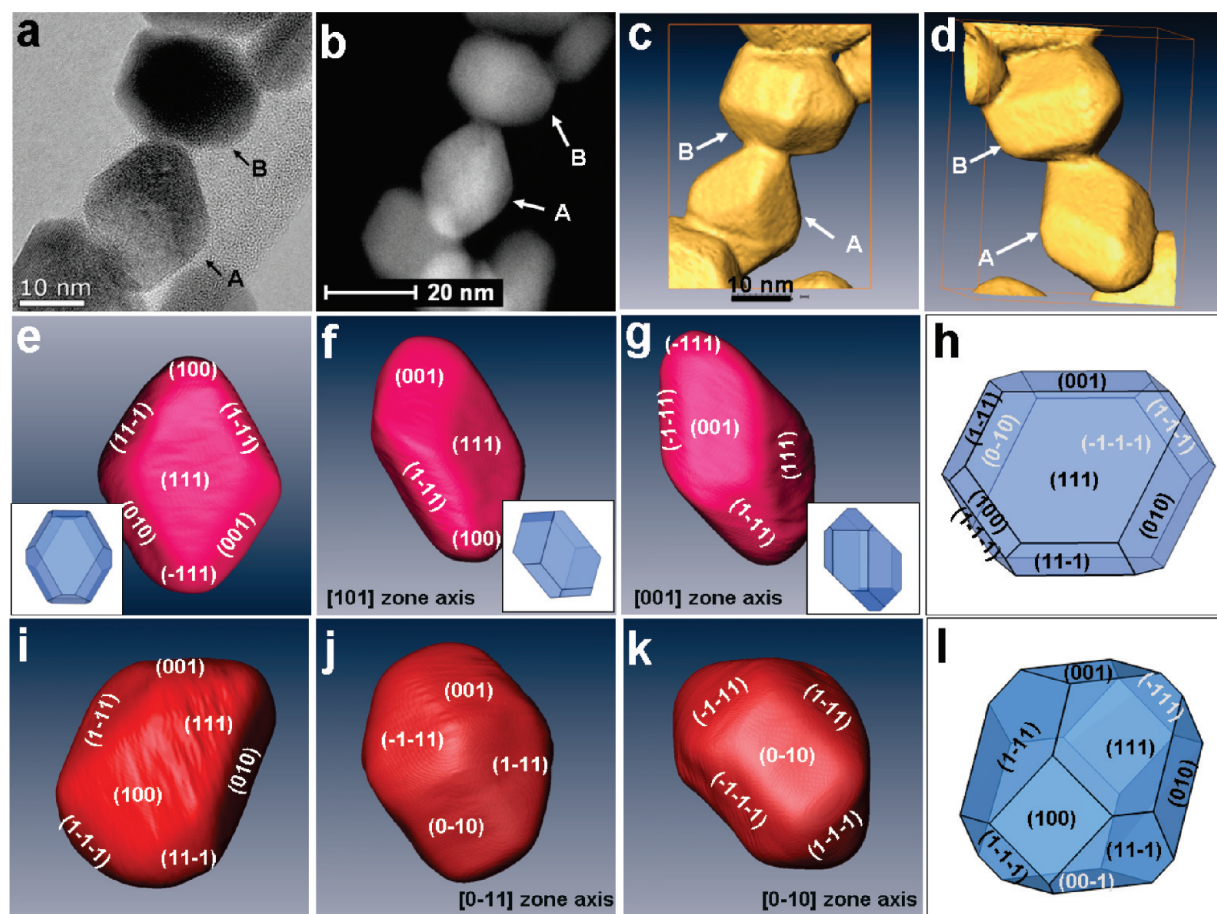


Figure 5. (a) Bright-field and (b) HAADF–STEM image of the same area containing large CeO_2 particles. (c) Top and (d) iso-surface rendering view of the reconstructed 3D volume of the particles. (e) Surface rendering view of particle A after segmentation viewed along (f) $[101]$ and (g) $[001]$. (i) Surface rendering view of particle B after segmentation and viewed along (j) $[0\bar{1}1]$ and (k) $[0\bar{1}0]$. (h, l) Corresponding schematic drawing of the structure of particles A and B.

(001) surfaces also changes with h ,

$$S(001) = 2h^2 \quad (2)$$

$$S(111) = 0.43L^2 - 2.60h^2 \quad (3)$$

Among the regular truncated octahedral structures, the cuboctahedron has the largest $\{001\}$ truncations. The corresponding area ratio of $S(001)$ to $S(111)$ is 2.3, indicating the dominant exposure of the $\{001\}$ facet on the cuboctahedron surface. Since the surface energy of the CeO_2 $\{001\}$ planes exceeds that of the $\{111\}$ planes by more than 1.73 times, the truncations should be as small as possible to reach a thermodynamically equilibrium shape. Thus, the corresponding ratios for $S(001)$, $S(100)$, and $S(010)$ to $S(111)$ for the particle depicted in Figure 2 are only 0.12, 0.12, and 0.04, respectively. The homogeneous growth environment in the solution and passivation of surfactants can be attributed to the growth of regular truncated octahedral CeO_2 nanocrystals shown in Figure 2.

However, it is important to note that the regular truncated octahedral shape is achieved only by sufficient surface diffusion or the dissolution and recrystallization process. The formation of different shapes of particles during the further hydrothermal process without PVP passivation is influenced by the combination of thermodynamic (the stabilities of different surfaces) and kinetic (the growth rates on these facets). Without protection of

the PVP on surface, the truncated octahedral CeO_2 particles tend to agglomerate during reaction by the formation of a coherent interface to minimize the interface energy. Because of the strong bond between Ce and O atoms, which leads to a limited diffusion rate when synthesized at a low temperature, a small fraction of regular truncated octahedra CeO_2 particles with large $\{001\}$ surfaces can form during the recrystallization and agglomeration process. A typical value of growth rate (a/b) of the particle in Figure 4a is 1.08, indicating deep truncations in the octahedron ($h/L = 0.26$) and a large area ratio ($S(001):S(111) = 0.57$).

Alternatively, to lower the total surface energy, irregular truncated octahedral CeO_2 particles are formed in greater abundance than that of the regular octahedron with deep $\{001\}$ truncations. From the thermodynamic point of view, the shrinkage of the $\{001\}$ surface proportions induces the evolution of the particles from regular octahedra with large truncations to compressed truncated octahedra. It is calculated that a cut parallel to the $(\bar{1}11)$ and $(1\bar{1}\bar{1})$ surfaces in Figure 4d (red color) can substantially reduce the areas of the three bounded $\{001\}$ planes as compared with that of the other three $\{111\}$ facets. For the particle in Figure 4b, the ratio of $S(001)$ to $S(111)$ is decreased dramatically to 0.28, compared with 0.70 for a regular truncated octahedron. This reduction to the proportion of $\{001\}$ facets on the surface would naturally stabilize the irregular truncated octahedral particles.

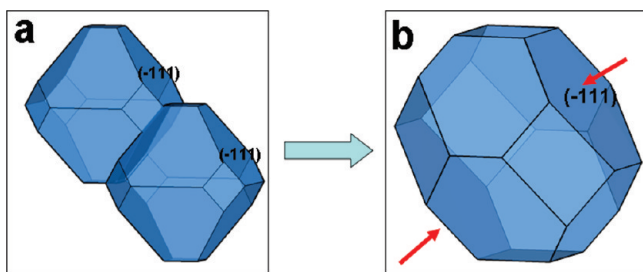


Figure 6. Schematic illustrations showing the aggregation and transformation from two fused regular truncated octahedral particles to a metastable irregular truncated octahedron.

From the kinetic viewpoint, without the protection of PVP molecules during the second part of the hydrothermal process, the small truncated octahedral CeO₂ particles obtained have a greater tendency to aggregate by sharing their common {111} or {001} surfaces to minimize the interfacial energy. The low surface diffusion and slow incorporation of atoms on the surface by step attachment will then transform the fused particles into a metastable irregular truncated octahedron instead of regular octahedron with large {001} truncations, which is described in Figure 6. Moreover, this metastable morphology not only is observed in samples prepared by hydrothermal methods, but also appeared frequently in samples synthesized by conventional coprecipitation followed by a high-temperature annealing treatment.^{30,32–34} The agglomeration of particles through a lattice matched coherent interface and subsequent low surface diffusion results in the formation of metastable compressed truncated octahedra during high-temperature annealing to suppress the exposed {001} facets. Even so, the area ratio of the {001} surface to the {111} surface is still higher than that of the regular and stable octahedral shape with small truncations. In general, the {001} facets of CeO₂ particles play an important role in catalytic reactions, such as the oxidation of CO and other volatile organic molecules.³⁰ From this result, we have confirmed that a higher ratio of reactive {001} facets can be generated during a high-temperature calcination process and high-temperature catalytic reactions. The formation of more {001} surface areas can be attributed to the favorable formation of an irregular metastable truncated octahedral structure by aggregation of small CeO₂ nanocrystals upon annealing.

4. CONCLUSION

In conclusion, the shapes and surface morphologies of CeO₂ nanocrystalline particles prepared using the hydrothermal method have been systematically studied with a tilt series of HRTEM images and 3D electron tomography. We believe the shape and corresponding kinetic mechanism of agglomeration for the CeO₂ discussed above are those typically seen in the synthesis of most CeO₂ nanocrystals in papers. The dominant shapes of these CeO₂ particles are the regular truncated octahedron and the irregular truncated octahedron, with preferred exposed {111} facets and small fractions of truncated {001} facets. The {001} type microfacets are observed on the {111} surface. Since CeO₂ nanoparticles with these two morphologies have also been observed frequently in the samples prepared by other methods, especially in commercial industrial products, the confirmation of their shape and morphology is very meaningful for the measurement of their corresponding chemical and physical properties and the establishment of their structure–catalytic property relationship.

■ ASSOCIATED CONTENT

S Supporting Information. A video clip is provided to show a 3D iso-surface rendering of particles A and B in Figure 5 after segmentation. Details of the Wulff construction of thermodynamically stable CeO₂ particles. Larger diffraction patterns of CeO₂ nanocrystals hydrothermally treated for 24 and 48 h. Magnified high-resolution TEM images of the particle in Figure 2 tilted to -30°, -20°, and 50°. This material is available free of charge via the Internet at <http://pubs.acs.org>.

■ AUTHOR INFORMATION

Corresponding Author

*E-mail: m-lin@imre.a-star.edu.sg.

■ REFERENCES

- Burda, C.; Chen, X. B.; Narayanan, R.; El-Sayed, M. A. *Chem. Rev.* **2005**, *105*, 1025–1102.
- Somorjai, G. A.; Park, J. Y. *Angew. Chem., Int. Ed.* **2008**, *47*, 9212–9228.
- Sun, Y. G.; Xia, Y. N. *Science* **2002**, *298*, 2176–2179.
- Ren, J. T.; Tilley, R. D. *J. Am. Chem. Soc.* **2007**, *129*, 3287–3291.
- Peng, Z. M.; Yang, H. *Nano Today* **2009**, *4*, 143–164.
- Tian, N.; Zhou, Z. Y.; Sun, S. G.; Ding, Y.; Wang, Z. L. *Science* **2007**, *316*, 732–734.
- Chen, M.; Kim, J.; Liu, J. P.; Fan, H. Y.; Sun, S. H. *J. Am. Chem. Soc.* **2006**, *128*, 7132–7133.
- Zhang, L.; Wu, J.; Liao, H.; Hou, Y.; Gao, S. *Chem. Commun.* **2009**, 4378–4380.
- Yuan, Q.; Duan, H. H.; Li, L. L.; Sun, L. D.; Zhang, Y. W.; Yan, C. H. *J. Colloid Interface Sci.* **2009**, *335*, 151–167.
- Yao, K. X.; Yin, X. M.; Wang, T. H.; Zeng, H. C. *J. Am. Chem. Soc.* **2010**, *132*, 6131–6144.
- Wang, Z. L. *J. Phys. Chem. B* **2000**, *104*, 1153–1175.
- Kwon, O.; Zewail, A. H. *Science* **2010**, *328*, 1668–1672.
- Li, H. Y.; Xin, H. L.; Muller, D. A.; Estroff, L. A. *Science* **2009**, *326*, 1244–1247.
- Kubel, C.; Voigt, A.; Schoenmakers, R.; Otten, M.; Su, D.; Lee, T. C.; Calsson, A.; Bradley, J. *Microsc. Microanal.* **2005**, *11*, 378–400.
- Weyland, M.; Midgley, P. A. *Mater. Today* **2004**, *32*–40.
- De Jone, K. P.; Koster, A. J. *ChemPhysChem* **2002**, *3*, 776–780.
- Andersson, B. V.; Herland, A.; Masich, S.; Inganäs, O. *Nano Lett.* **2009**, *9*, 853–855.
- van Bavel, S. S.; Sourty, E.; de With, G.; Loos, J. *Nano Lett.* **2009**, *9*, 507–513.
- Ersen, O.; Parmentier, J.; Solovyov, L. A.; Drillon, M.; Pham-Huu, C.; Werckmann, J.; Schultz, P. *J. Am. Chem. Soc.* **2008**, *130*, 16800–16806.
- Trovarelli, A. *Catalysis by Ceria and Related Materials*; Imperial College Press: London, 2002, pp 1–528.
- Trovarelli, A.; de Leitenburg, C.; Boaro, M.; Dolcetti, G. *Catal. Today* **1999**, *50*, 353–367.
- Kaspar, J.; Fornasiero, P.; Graziani, M. *Catal. Today* **1999**, *50*, 285–298.
- Steele, B. C. H. *Nature* **1999**, *400*, 619–621.
- Steele, B. C. H.; Heinzel, A. *Nature* **2001**, *414*, 345–352.
- Liu, X.; Yin, S.; Sato, T. *Mater. Sci. Eng.* **2009**, *1*, 012013.
- Li, R. X.; Yabe, S.; Yamashima, M.; Momose, S.; Yoshida, S.; Yin, S.; Sato, T. *Solid State Ionics* **2002**, *151*, 235–241.
- Baudin, M.; Wojcik, M.; Hermansson, K. *Surf. Sci.* **2000**, *468*, 51–61.
- Sayle, T. X. T.; Parker, S. C.; Sayle, D. C. *Chem. Commun.* **2004**, 2438–2439.
- Zhang, F.; Jin, Q.; Chan, S. W. *J. Appl. Phys.* **2004**, *95*, 4319–4325.

- (30) Aneggi, E.; Llorca, J.; Boaro, M.; Trovarelli, A. *J. Catal.* **2005**, 234, 88–95.
- (31) Feng, X. D.; Sayle, D. C.; Wang, Z. L.; Paras, M. S.; Santora, B.; Sutorik, A. C.; Sayle, T. X. T.; Yang, Y.; Ding, Y.; Wang, X. D.; Her, Y. *Science* **2006**, 312, 1504–1508.
- (32) Wang, Z. L.; Feng, X. D. *J. Phys. Chem. B* **2003**, 107, 13563–13566.
- (33) Hu, C.; Zhang, Z.; Liu, H.; Gao, P.; Wang, Z. L. *Nanotechnology* **2006**, 17, 5983–5987.
- (34) Yuan, Q.; Duan, H. H.; Li, L. L.; Sun, L. D.; Zhang, Y. W.; Yan, C. H. *J. Colloid Interface Sci.* **2009**, 335, 151–167.
- (35) Mai, H. X.; Sun, L. D.; Zhang, Y. W.; Si, R.; Feng, W.; Zhang, H. P.; Liu, H. C.; Yan, C. H. *J. Phys. Chem. B* **2005**, 109, 24380–24385.
- (36) Kaneko, K.; Inoke, K.; Freitag, B.; Hungria, A. B.; Midgley, P. A.; Hansen, T. W.; Zhang, J.; Ohara, S.; Adscharit, T. *Nano Lett.* **2007**, 7, 421–425.
- (37) Yang, S. W.; Gao, L. *J. Am. Chem. Soc.* **2006**, 128, 9330–9331.
- (38) Zhou, K.; Wang, X.; Sun, X.; Peng, Q.; Li, Y. *J. Catal.* **2005**, 229, 206–212.
- (39) Si, R.; Flytzani-Stephanopoulos, M. *Angew. Chem., Int. Ed.* **2008**, 47, 2884–2887.
- (40) Wulff, G. *Z. Krystallogr. Mineral.* **1901**, 34, 449–530.